

Chemical Prelithiation of Silicon Powder and its Role as Anode Material for All-Solid-State Batteries

Tobias Neumann,* Alain Thomas Cerny, Svenja Kalthoff, Lea Eisele, Ingo Krossing, and Sonia Dsoke*

Silicon (Si) is a high-capacity material, which faces substantial volume changes during de-/lithiation, leading to severe degradation of the battery. Chemical prelithiation is a promising strategy to enhance the performance of Si anodes in lithium (Li)-ion based all-solid-state batteries (ASSB) by mitigating these volume changes and improving cycling stability. In this article, the possibility of the prelithiation of Si powder using a lithium–arene complex solution with subsequent recovery of the arene and solvent is explored. Using a variety of physiochemical analysis methods, like attenuated total reflection infrared spectroscopy, Raman spectroscopy, inductively coupled plasma optical emission spectroscopy, and soft

X-ray emission spectroscopy, the success of an inhomogeneous prelithiation is confirmed. To study the electrochemical performance (galvanostatic cycling, electrochemical impedance spectroscopy) of the material, the obtained material is integrated in form of a casted electrode into a sulfide-based ASSB cell setup using a thin separator layer ($\approx 30\ \mu\text{m}$) and a casted $\text{LiNi}_{0.6}\text{Mn}_{0.2}\text{Co}_{0.2}\text{O}_2$ (NMC622) cathode, and the findings is compared with thus of a casted Si anode. The obtained data reveal the enhanced cycle stability prelithiated Si exhibits under certain condition, proving the benefits of this chemical prelithiation approach for next-gen anodes in Li-ion battery applications.

1. Introduction

All-solid-state Batteries (ASSB) are emerging as future energy storage systems, offering enhanced safety and potentially higher energy densities compared to conventional lithium (Li)-ion batteries (LIB).^[1–3] The defining distinction lies in the substitution of liquid electrolytes with solid ones, which not only introduces new advantages but also challenges in the design and operation of these batteries. Solid electrolytes can be classified into various material classes. Each material class exhibits different properties that can be favorable for various performance and application requirements. Thiophosphates (sulfides) being one of them, possess high ionic conductivities (up to $10^{-2}\ \text{S cm}^{-1}$) at room

temperature and promising mechanical properties, such as high ductility, making them favorable for densification procedures upon cell fabrication.^[4–6]


By incorporating solid electrolytes into electrodes, porosity can be filled out, enabling sufficient transport pathways for Li-ions and a high ionic conductivity throughout the entire electrode structure. This generally leads to increased rate capability, but however, reduced energy densities due to the inactive solid electrolyte content in the electrodes. To maximize the energy density, electrolyte-free electrode designs are studied with great interest.^[7] For anodes, Li metal anodes are the dominating focus of current research. Nevertheless, the application of Li metal anodes is still hindered, for example, with severe dendrite formation eventually leading to cell malfunction. Therefore, alternative anode active materials with high capacity and low working potential must be investigated.^[8]


Silicon (Si) has emerged as a prominent anode material for LIBs and especially ASSB due to its low voltage for an anode and high theoretical specific capacity of $\approx 3570\ \text{mAh g}^{-1}$ ($\text{Li}_{15}\text{Si}_4$), significantly surpassing that of conventional graphite ($\approx 372\ \text{mAh g}^{-1}$).^[7,9–11] However, its severe volume expansion ($>300\%$) upon lithiation induces stress and causes cracking and pulverization, leading to rapid capacity fading and cycling instability.^[10–12] Reducing the particle size to micro- and nanometer scale, encapsulating the Si material into a carbon matrix or designing nanostructured Si materials, can reduce the impact of volume change effectively and increase the cycle life of Si anodes greatly.^[12,13] However, solid–electrolyte interphase (SEI) stability remains a major challenge since the SEI gradually forms during (de-)lithiation as surfaces repeatedly break up and expose fresh Si surface. Various strategies have been proposed to mitigate the degradation of Si and ensure higher cycling stability, with prelithiation being one of them.^[14,15] Prelithiation describes the incorporation of Li into an active material prior to

T. Neumann, A. T. Cerny, S. Kalthoff, L. Eisele, S. Dsoke
 Department of Electrical Energy Storage
 Fraunhofer Institute for Solar Energy Systems ISE
 Heidenhofstraße 2, 79110 Freiburg, Germany
 E-mail: tobias.neumann@ise.fraunhofer.de
 sonia.dsoke@ise.fraunhofer.de

I. Krossing
 Institute for Inorganic and Analytical Chemistry (IAAC)
 University of Freiburg
 Albertstraße 21, 79104 Freiburg, Germany

S. Dsoke
 Department of Sustainable Systems Engineering (INATECH)
 Faculty of Engineering
 University of Freiburg
 Emmy-Noether-Straße 2, 79110 Freiburg, Germany

 Supporting information for this article is available on the WWW under <https://doi.org/10.1002/batt.202500332>

 © 2025 The Author(s). Batteries & Supercaps published by Wiley-VCH GmbH. This is an open access article under the terms of the Creative Commons Attribution License, which permits use, distribution and reproduction in any medium, provided the original work is properly cited.

the first formation cycle of a battery cell. The primary motivation behind this regarding Si is to improve the initial Coulombic efficiency and electrochemical performance of the anodes by preemptively addressing the volume expansion issues and enhancing the overall active Li content.^[14–17] Prelithiation can help stabilize the SEI formation during the initial cycles, thereby prolonging the lifespan of the anode.^[18,19] Furthermore, prelithiation serves to counterbalance the Li loss that typically occurs during the first charge cycle, facilitating a more efficient utilization of silicon's high capacity.

Prelithiation of silicon can be performed via a variety of methods, which are typically divided into electrochemical and chemical approaches. In the electrochemical approach, lithiation is driven by the electrochemical lithiation potential of Si. The lithiation can take place either in a controlled environment by using half cells or by directly contacting a lithium foil (or other lithium sources) with the anode, which results in a short circuit between both layers when electrolyte is added. For the chemical approaches, lithiation mainly occurs due to the high chemical potential of Li metal, forcing the formation of Li–Si alloys. Several methods have been proposed in the recent years.^[18–21]

1) Mechanical alloy method: Mixing Li metal and Si using a ball-milling machine. 2) Direct contact method: Pressing Li metal foil onto a Si anode layer. 3) One-pot metallurgical method: Stirring Si in molten Li metal. 4) Physical vapor deposition: Evaporation of the Li metal and deposition onto the Si.

Besides these methods, another way to perform chemical prelithiation involves the introduction of a carrier molecule capable of forming an intermediate with lithium metal. Depending on the selected carrier, the intermediate can be designed to achieve a specific chemical lithiation potential, which enables a similar control over the degree of lithiation (DOL) as that achieved by electrochemical prelithiation in half cells. One of the most common ways to conduct this type of prelithiation involves the formation of a lithium–arene complex (LAC) solution, using the arene as the carrier molecule.^[19] Jang et al., for example, successfully applied this method on Si/SiO₂ electrodes for classic LIB using various biphenyl derivatives in 1,2-dimethoxyethane (DME) as LAC.^[14] They found that the selected arene directly affects the thermodynamical conditions for the lithiation and can therefore be used to achieve different DOL. Additional studies, for example, by Choi et al. also demonstrated the role of the solvent in this regard.^[15,22] They showed that ion–pair interaction with the solvent is directly linked to the used solvent. By selecting solvents with different solvating power in form of DME and tetrahydropyran (THP) in combination with biphenyl (BP) as arene, they were able to demonstrate the formation of a solvent-separated and a contact ion pairs (CIP), respectively. As a result they were able to demonstrate that the CIP was beneficial for the prelithiation of graphite, which was also confirmed by Shen et al., who used tetrahydrofuran (THF) and 2-methyltetrahydrofuran as solvents.^[15,23]

Following this approach, herein, we present our most recent findings on a sustainable route for partial prelithiation of microcrystalline silicon (μ -Si) powder and its integration into ASSB. Utilizing the powder form the focus ensures a potential scalable solution (as

demonstrated by Kuo et al.).^[24] For the LAC system, we chose 3,3',4,4'-tetramethylbiphenyl (TMBP) in THF to ensure improved prelithiation conditions capable to reach high DOL. To enhance the strategy in terms of cost-effectiveness and sustainability, we significantly reduced the amount of used TMBP ($n(\text{Li})/n(\text{TMBP}) = 50$), thereby forcing the TMBP to function as a carrier. To maintain a storage capacity of at least 2 Li per Si, we limited the amount of used Li to reach a DOL of 0.5 ($\text{Li}_{0.5}\text{Si} = 476 \text{ mAh g}_{\text{Si}}^{-1}$). The finished powder was obtained using evaporation methods, enabling us to recover the used THF and TMBP and rendering the process waste-free.

Besides physicochemical (Raman, attenuated total reflectance infrared [ATR-IR], scanning electron microscopy [SEM], soft X-ray emission spectroscopy [SXES]) investigations to confirm the successful prelithiation, the material was used to prepare electrolyte-free electrodes using a slurry casting approach. These electrodes are compared to pristine Si electrodes in regards of their microstructural changes using SEM-SXES as well as electrochemical properties inside an ASSB cell using electrochemical impedance spectroscopy (EIS), galvanostatic cycling as well as C-rate capability testing. For the assembly of the ASSB cells, $\text{Li}_6\text{PS}_5\text{Cl}$ (LPSCI) infiltrated into a nonwoven scaffold was used as thin layer separator ($\approx 30 \mu\text{m}$) and a slurry casted blend of $\text{LiNi}_{0.6}\text{Mn}_{0.2}\text{Co}_{0.2}\text{O}_2$ (NMC622) and LPSCI was used as cathode. The areal density of the electrodes was adjusted to enable an electrochemical (de-) lithiation of 2 Li per Si during cycling without exceeding an overall DOL of 3.5. By limiting the DOL, effects associated with higher DOL (e.g. formation of the crystalline phase $\text{Li}_{15}\text{Si}_4$) can be mitigated, which benefits microcrystalline Si as demonstrated by Graf et al.^[25]

2. Results and Discussion

2.1. Prelithiation of Silicon

For the prelithiation of Si, a prelithiation solution was prepared by adding Li metal grains to a TMBP:THF solution (Figure 1). Instantaneous, a blue coloring immersed from the Li chunks,

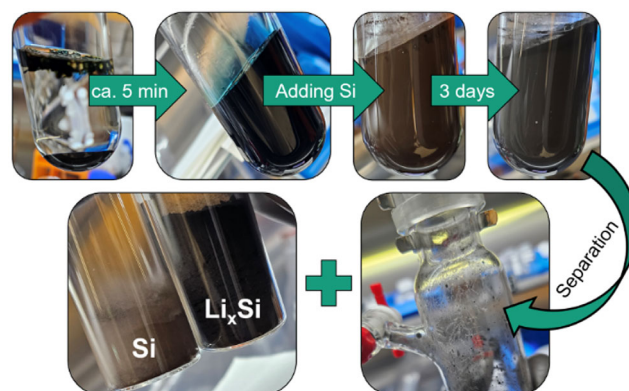
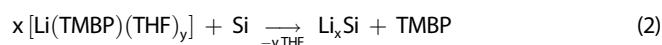
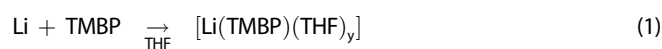


Figure 1. Chemical prelithiation process of μ -Si. In the last step crystals of TMBP are formed at the wall of the vessel and the residual Li_xSi powder is compared to the pristine Si powder.

signaling the formation of the $[\text{Li}(\text{TMBP})(\text{THF})_y]$ complex. After a few minutes, the complete solution turned dark blue, indicating the complete activation of the TMBP. Adding pristine Si powder resulted in the fading of the overall blue color. However, changes in coloring still occurred around the Li chunks, indicating the continuous formation of the LAC. Upon completion of the reaction, all Li chunks have disappeared, and the former brownish dispersion turned black, indicating a change of the material composition.

Removing the liquid phase *i. vac.* and treatment of the residual powder at elevated temperature resulted in the formation of colorless crystals inside the vessel, which were identified as TMBP (see Figure S1, Supporting Information). The remaining black powder visually indicates the success of the prelithiation procedure, particularly given its vicious reaction upon contact with H_2O (see Figure S2, Supporting Information).

Based on the studies conducted by Choi et al. and Shen et al., the prelithiation mechanism might have occurred as follows. First, the Li formed in combination with TMBP and THF, a $[\text{Li}(\text{TMBP})(\text{THF})_y]$ complex (Equation (1)), which when in contact with Si formed the Li_xSi alloy, releasing the TMBP carrier and THF (Equation (2)). Since per 50 Li, only one TMBP was present, the two reactions repeated until all Li was consumed.



For further investigation, electrodes were formed from the obtained and pristine powder (Figure S3, Supporting Information). Similar to the powders, the casted electrodes differ from each other. The Si electrode appears in a metallic glance after processing, which is a notable change from the brownish powder, but shows the high-quality of the Si. The Li_xSi electrode, however, appears similar to the Li_xSi powder, indicating the persistence of prelithiation even after processing.

For investigation of potential impurities and changes of the material after the prelithiation and slurry casting process, ATR-IR (Figure S4, Supporting Information) and Raman (Figure 2) spectra of the Li_xSi electrode were measured and compared to the Si electrode. Due to a lack of strong signals in both cases, the ATR-IR spectra mainly consist of background noises with the exception

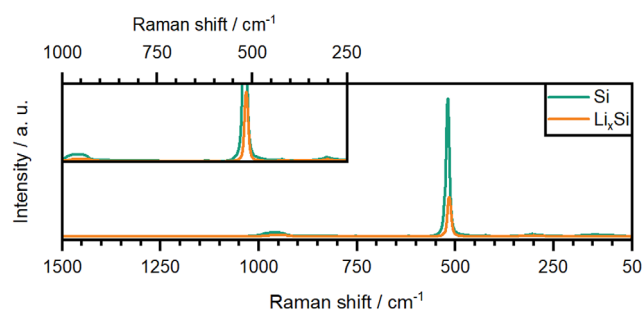


Figure 2. Raman spectra of Si electrode (green) and Li_xSi electrode (orange) acquired using the same measurement parameters. Inset: Magnification of the data.

of low intensity signals for hydrogenated nitrile butadiene rubber (HNBR) (2928 , 2856 , and 1464 cm^{-1}) binder detected in the Si electrode, displaying that no side products were formed during the whole process.^[26]

Comparison of both Raman spectra (Figure 2) presents the characteristic Si signal at 519 cm^{-1} accompanied by the overtones at 303 and 966 cm^{-1} . However, in case of the Li_xSi electrode, these signals are strongly decreased with the overtones disappearing almost completely. The decrease in intensity can reflect a loss in crystallinity and occurs due to the incorporation of Li into the Si lattice. Even though this data does not provide direct confirmation of the successful prelithiation, the absence of Si–O vibrations highlights not only the high purity of the Si but also the successful mitigation of side reactions during the process. To confirm the success of the prelithiation procedure, parts of the Li_xSi electrode were exposed to normal atmosphere, allowing for decomposition to occur. Analyzing the decomposed Li_xSi anode with ATR-IR spectroscopy (Figure 3) revealed multiple vibration signals.

The signals at 1411 and 860 cm^{-1} reflect the asymmetric stretching (ν_{as}) and out-of-plane bending (δ) modes of carbonate (CO_3^{2-}) and indicate the formation of Li_2CO_3 .^[27] Interestingly, the additional broad signals between 1000 and 1200 cm^{-1} are referring to Si–O–Si vibrations.^[28,29] Since these signals are undetectable for the reference Si electrode, their appearance indicates an increased reactivity of the Si inside Li_xSi electrode, which matches with the existence of a highly reactive Li–Si alloy.

Although the successful prelithiation was indirectly proven via ATR-IR and Raman spectroscopy, locating Li_xSi via SEM-SXES can provide direct evidence on the success of the prelithiation and additional information regarding the homogeneity of lithiation. Figure S5, Supporting Information, presents a top-view SEM image of the Li_xSi anode, along with the grid points measured for SXES analysis. The SXE spectra (Figure 4, S5, Supporting Information) of all spots show significant differences in the Li–K and Si– $L_{2,3}$ regions and can, in some cases, contain additional weak signals above 100 eV , mainly related to oxygen, indicating the existence of surface impurities. Some spots (P01, P06) show no or barely any Li–K signal (Li metal = 54.2 eV) and a Si– $L_{2,3}$ signal consisting of two peaks at 89.5 eV (3s component) and 91.8 eV (3p component) as well as a broad shoulder around 96 eV , which is characteristic for crystalline Si as shown by Aoki et al., signaling that no or not enough lithiation occurred to induce a change in the Si lattice.^[30,31] Others (P07, P10, P15), however, reveal a strong Li–K signal shifted to lower eV compared to Li metal and are accompanied by a

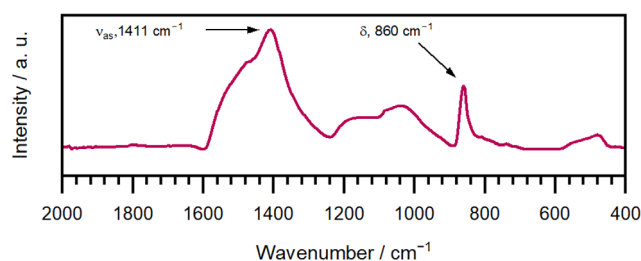


Figure 3. ATR-IR spectrum of Li_xSi electrode after exposure to air for 48 h.

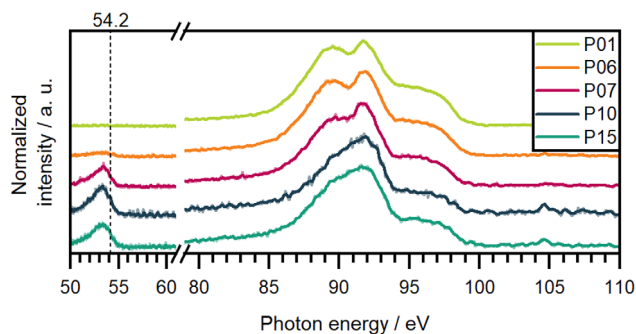


Figure 4. SXE spectra of Li_xSi electrode. The spectra are normalized to the highest individual value and the lines are smoothed via a moving average.

change of the $\text{Si-L}_{2,3}$ signal. The shift of Li-K , typically to 53.5 eV, clearly demonstrates the integration of Li into Si as shown by Lin et al.^[31] The amount of integrated Li can thereby be estimated by the shape of the Si signal. For P07, for example, a Li-K signal can be found at 53.4 eV, but the $\text{Si-L}_{2,3}$ region still resembles that of crystalline Si, indicating a low DOL.

The Li-K signal of P10 and P15, however, is also located in this area (53.3 eV), but shows significant changes in the $\text{Si-L}_{2,3}$ region. Instead of two peaks, the Si signal of P10 and P15 only consists of one distinct peak at 91.9 eV, which, however, is still accompanied by an indistinguishable one at lower photon energy as well as a broad shoulder around 96 eV. Since this changes to the Si signal combined with a Li-K to $\text{Si-L}_{2,3}$ ratio of 0.34 (P15) and 0.42 (P10) deviate from reported SXE spectra of highly lithiated Si, like $\text{Li}_{13}\text{Si}_4$ (DOL = 3.25) and $\text{Li}_{15}\text{Si}_4$ (DOL = 3.75), it can be assumed that no Li-Si alloy exceeding a DOL of 3 was formed during the prelithiation. In total, this data show that prelithiation occurred quite inhomogeneous inside the sample. The reason for the inhomogeneous prelithiation is most likely a product of the chosen arene:solvent combination. Since the high chemical potential of $[\text{Li}(\text{TMBP})(\text{THF})_y]$ does not limit the DOL to 0.5, no thermodynamic restrictions were present to prevent the lithiation beyond a DOL of 0.5. Therefore, the process was only limited by kinetic conditions, which, as shown by SXES analysis, allowed for the excessive consumption of Li by certain Si particles and resulted in an inhomogeneous lithiation. However, to assess the amount of accessible Li, inductively coupled plasma optical emission spectroscopy (ICP-OES) was conducted. For this, Li_xSi powder was quenched in water and filtered to remove residual powder. The measurement revealed

a Li concentration in the aqueous solution (measured: 8.46 mg l^{-1} , expected: 11 mg l^{-1}) that was 23% smaller than the theoretical calculated value. Surprisingly, the incurred loss of Li is greater than the expected margin of error, indicating that some of the Li might remained trapped inside the Si particles or formed water-insoluble species, like lithium silicates (Li_ySiO_z), during the quenching procedure.

2.2. Microstructural Investigation

To assemble the ASSB cell, the individual layers (cathode/separator/anode) were joined and tightly compacted to ensure good connection between the different particles. A cross-section of the cell stack with an integrated Li_xSi or Si anode is shown in **Figure 5**. As shown in the overview (Figure 5A,C) both cells were assembled using similar cathodes and separators. The cathodes are comprised of an interpenetrating network of NMC622 and LPSCI particles as displayed by the individual element images (Figure S6, S7, Supporting Information) and their thicknesses are measured to be $\approx 47 \mu\text{m}$ (Si anode) and $53 \mu\text{m}$ (Li_xSi anode). The resulting density is, in both cases, between 3.0 and 3.1 g cm^{-3} , demonstrating the similarity of the used cathodes. The differences in thickness are within the margin of error as shown in the Experimental Section. The incorporated separators are comprised of LPSCI particles and a PET nonwoven scaffold and are $\approx 32 \mu\text{m}$ in thickness. Both electrodes exclusively face LPSCI on the electrode/separator interfaces, which ensures not only a good connection between the layers but also a homogeneous Li transport between them.

The main differences between both cell stacks can be found in the anode layers, which (excluding the binder) consist solely of Si or Li_xSi and measure $10.5 (+0.5/-0.8) \mu\text{m}$ (Si) and $9.0 (+0.4/-0.4) \mu\text{m}$ (Li_xSi) in thickness. While at low magnification both layers show no significant difference, distinct particle distribution inside the electrode is revealed at high magnification (Figure 5B,D). In case of the pristine Si electrode, the particles size ranges between 0.1 and $1.0 \mu\text{m}$ and voids can be detected throughout the layer. Inside the Li_xSi electrode, the particle size distribution appears similar, however, the visible voids are drastically reduced, resulting in a tightly packed layer with discernible particle edges. This kind of response to densification is caused by a change in hardness of the particles surfaces due to formation of the Li-Si alloy.^[32]

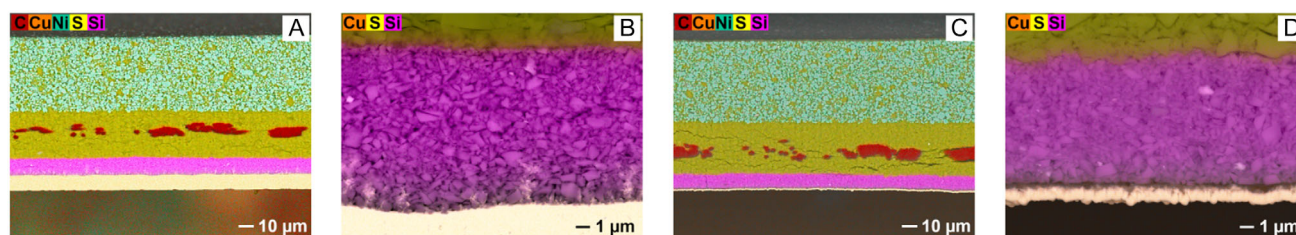


Figure 5. Ion-polished cross-section SEM images in combination with EDX mapping of an assembled ASSB cell with Si and Li_xSi anode in A,C) low magnification and B,D) high magnification focusing on the anode layer. The individual elements are colored red (carbon), orange (copper), green (nickel), yellow (sulfur), and purple (silicon).

2.3. Battery Cell Data Analysis

To investigate the effect of prelithiation on the cell performance, ASSB cells were assembled as described in the Experimental Section. The electrochemical evaluation was conducted via galvanostatic and EIS measurements, using matching pristine Si (Si-cell) and Li_xSi (Li_xSi -cell) electrodes, which enable a transfer of $\approx 2e^-$ per Si during cycling. The galvanostatic measurements were divided into different segments: formation at 0.2 C, cycling at 2 C, C-rate capability testing (0.5–8 C), and cycling at 4 C to enforce ageing (rapid ageing). To adapt for differences in the Si half-cell potential caused by the prelithiation, the upper

cut-off voltage was set to 4.2 and 4.25 V for analyzing pristine Si and Li_xSi anodes, respectively. The galvanostatic part of the electrochemical evaluation is shown in Figure 6 and 7. During the formation step, the charging curves of both cells (Figure 6A) are almost indistinguishable from each other. The primary difference is caused by the adjusted cut-off voltage leading to different spec. charging capacities (Q_{Ch}) of 209.8 and 217.6 $\text{mAh}\cdot\text{g}_{\text{NMC622}}^{-1}$ for the Si-cell and Li_xSi -cell, respectively.

This deviation is mainly caused by the one-time occurring pseudo-plateau of Si between 0.10 and 0.04 V (vs. Li/Li^+ , $\text{DOL} = 0.5\text{--}3$) during first lithiation and indicates that the cathode of the Li_xSi -cell was slightly more delithiated.^[33] Upon

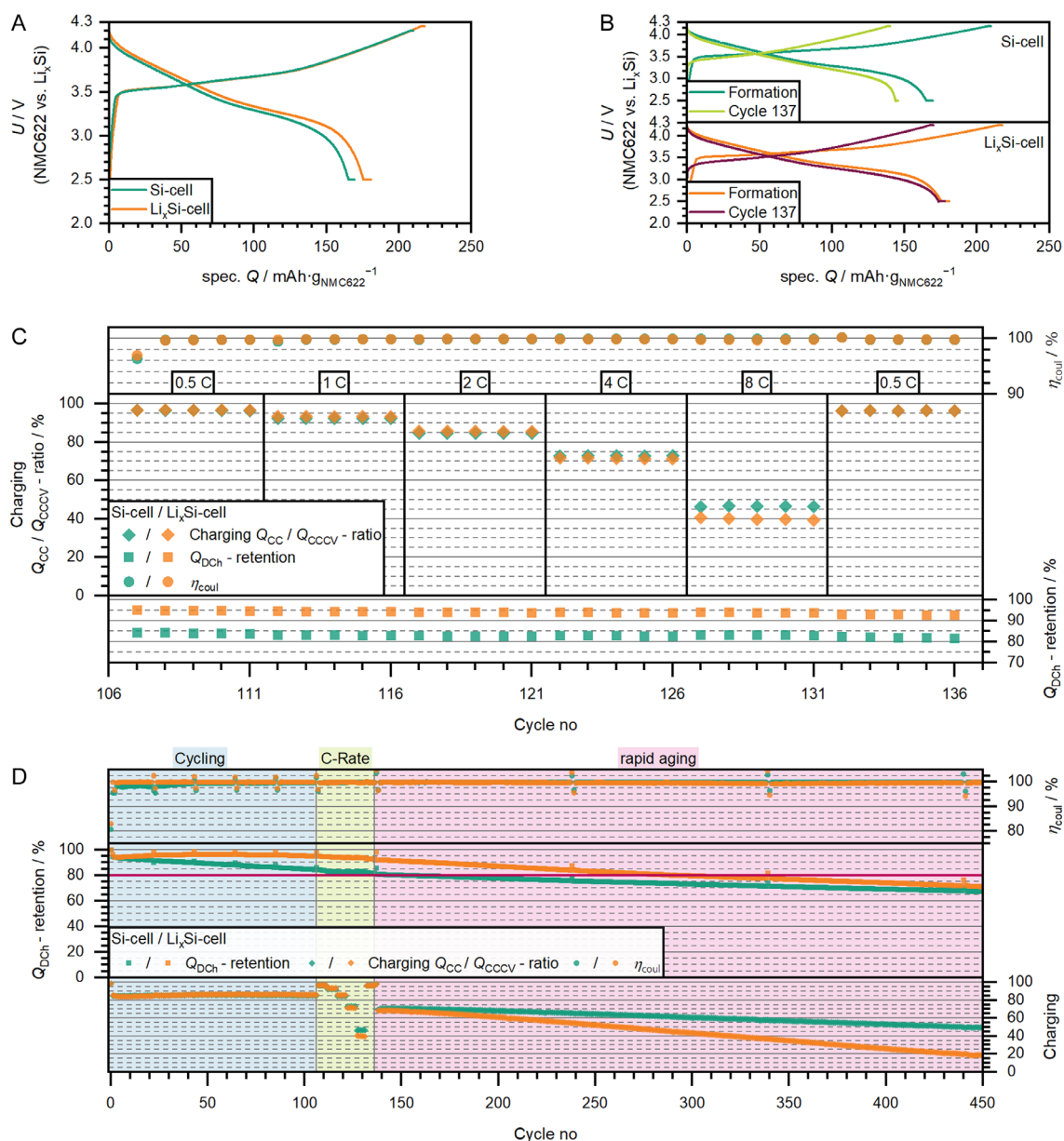


Figure 6. Electrochemical evaluation of Si-cell (green) and Li_xSi -cell (orange). Voltage curve (voltage vs. capacity) of the A,B) formation and (B) cycle 137 normalized to the respective NMC622 content. C) C-rate capability test results ranging from C-rates of 0.5–8 C. D) Overview of the cycle life stability (separated in the regions of cycling at 2 C, C-rate capability testing and rapid ageing at 4 C represented by the Q_{DCh} -retention, charging $Q_{\text{CC}}/Q_{\text{CCCV}}$ -ratio, and Coulombic efficiency (η_{coul}). Cells were tested at 50 °C and achieved an areal discharge capacity (based on the area of the cathode) of 1.94 mAh cm^{-2} (Si-cell) and 2.09 mAh cm^{-2} (Li_xSi -cell) during formation.

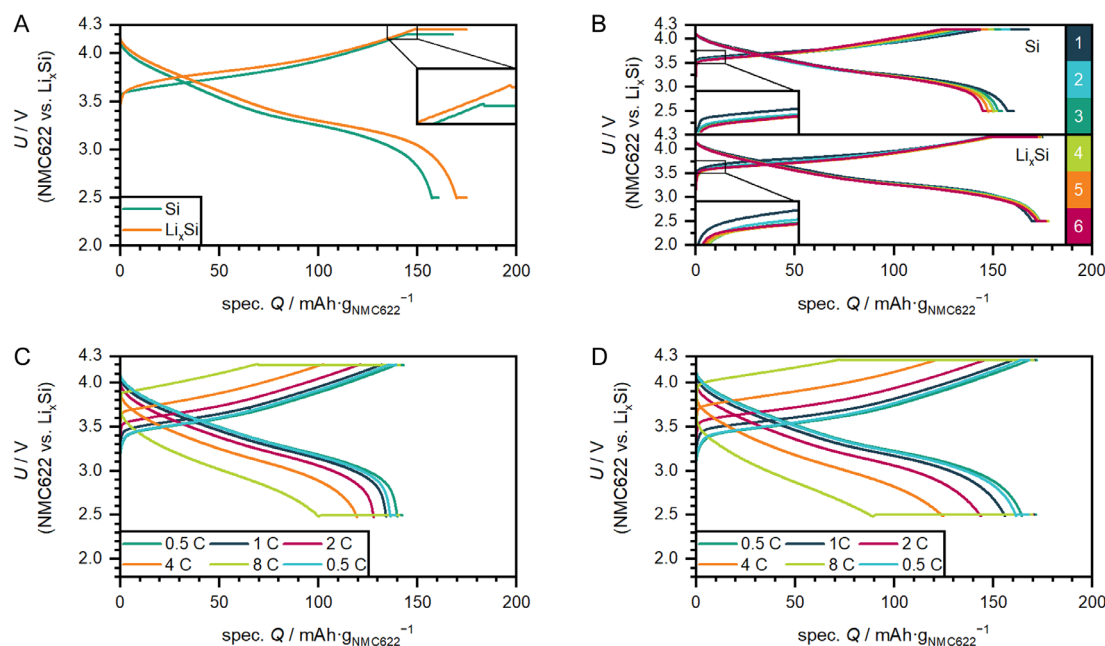


Figure 7. A) Voltage curve of Si-cell (green) and Li_xSi-cell (orange) during the 1st energy test. B) Voltage curves of Si-cell (above) and Li_xSi-cell (below) for all six energy tests during the cycling period. C,D) Voltage curves of (C) Si-cell and (D) Li_xSi-cell during C-rate capability testing (displayed is the 3rd cycle of each step in respective order: 0.5, 1, 2, 4, 8, and 0.5 C). The capacity was in all cases normalized to the respective NMC622 content.

discharging, the cells retained capacities of $169.6 \text{ mAh}\cdot\text{g}_{\text{NMC622}}^{-1}$ (Si-cell) and $180.8 \text{ mAh}\cdot\text{g}_{\text{NMC622}}^{-1}$ (Li_xSi-cell), equating to a Coulombic efficiency (η_{coul}) of 80.81% and 83.12%, respectively, for the formation. When excluding the additionally obtained capacity during charging, a gap of $\approx 3 \text{ mAh}\cdot\text{g}_{\text{NMC622}}^{-1}$ remains between the cells after discharging, which indicates the capability of Li_xSi to reduce the impact of side reaction during formation. In the beginning of the 2 C cycling period (1st energy test), both cells face a significant drop in Q_{DCh} -retention. While the Si-cell dropped to 94.7% in this process, 96.6% was maintained by the Li_xSi-cell upon comparing the voltage curves (Figure 7A,B) of the energy tests, the Li_xSi-cell shows an increased potential up until 4.20 V, at which both charging patterns nearly overlap. This causes the mean charging voltage (3.95 V) of the Li_xSi-cell to be increased compared to the Si-cell (3.89 V). When examining the region of the cut-off potential in detail (Figure 7A, inset) a small deviation of the spec. Q_{Ch} is noticeable at 4.20 V. The amount ($\approx 3 \text{ mAh}\cdot\text{g}_{\text{NMC622}}^{-1}$) is equal to the above-mentioned and substantiate the need for the adjusted cut-off voltage in case of the Li_xSi-cell, even though 4.22 V would have been more fitting when comparing the data. The η_{coul} of 1st energy test is 99.88% for the Li_xSi-cell and 95.63% for the Si-cell, indicating that a significant amount of Li trapping only occurs in the Si-cell.

Upon initiating the 2 C dis-/charging cycle (Figure 6D), both cells drop to a Q_{DCh} -retention of $\approx 94\%$, which was caused by the change in cut-off current to 0.2 C. The ratio of charged capacity achieved during constant current and total achieved capacity ($Q_{\text{CC}}/Q_{\text{CCCV}}$ -ratio) is in both cases almost identical at 85%, showing that the limit for charging at 2 C in both cases is not affected by presence of prelithiation. Upon completion of the 6th energy test (end of the 2 C cycling period), the Si-cell is retained only 86.3% of the initial Q_{DCh} . However, since the charging $Q_{\text{CC}}/Q_{\text{CCCV}}$ -ratio

remained almost the same over this time, ageing seems not to be linked to a restricted Li-ion transport, but rather is caused by the loss of active Li as indicated by the reduced η_{coul} , which experienced a steady increase (from 98.2% to 99.7%, excluding energy tests) in that period. The Li_xSi-cell, however, shows a completely different ageing profile. Even though the cell experienced a significant loss after formation, most of this capacity was recovered during the first part of the cycling, finishing the test at 97.6% (6th energy test). During the 3rd energy test a maximum of 98.5% in Q_{DCh} -retention was reached, marking the immense impact of Li_xSi material on the cell stability. However, analyzing the evolution of the η_{coul} the value remained around 99.97% (energy tests excluded) in the first part and declined to 99.90%, when the Q_{DCh} -retention started to fade. The reason for this response can, therefore, not be explained by the access to the preliminary integrated active Li, but rather by a change in the charging pattern of the Li_xSi-cell.

When investigating the individual energy tests (Figure 7B), the charging pattern of the Li_xSi-cell changes significantly. While charging of the 1st energy test started ($10 \text{ mAh}\cdot\text{g}_{\text{NMC622}}^{-1}$) at elevated voltages (3.67 V), starting voltage of the 2nd energy test already dropped to 3.62 V and continued to drop till the 3rd energy test, causing a reduction of the mean charging voltage to 3.90 V. A similar (but weaker effect) can also be observed for the Si-cell (Figure 7B), implying that the change is caused by the restructuring of the anode. During this process, former nonaccessible Si or Li_xSi is being connected, resulting in an increase of the Si lithiation potential, and consequently, a drop of the overall cell voltage. Since this event is occurring in both cases, the main difference affecting ageing is caused by the preliminary integrated Li. This ensures that no electrochemical active Li needs to be consumed to stabilize the restructuring, which

explains the huge gap in Q_{DCh} -retention for Li_xSi -cell (97.6%) and Si-cell (86.3%) after the cycling period.

After the cycling period, C-rate capability testing (Figure 6C) at 0.5, 1, 2, 4, and 8 C was conducted on both cells to analyze the response to the adjusted current densities. At the beginning of the test, a small drop in η_{coul} is noticeable, which as shown before, is connected to the change in cut-off current to 0.2 C for the C-rate capability testing. Apart from that no significant effects can be seen up until 8 C. Both cells reacted likewise to the applied currents and were able to achieve a charging Q_{CC}/Q_{CCCV} -ratio of 96.6% (0.5 C), 93.4% (1 C), 85.8% (2 C), and 73.0% (4 C) with minor deviations ($\approx 1\%$) from 0.5 till 2 C (Si-cell) and 4 C (Li_xSi -cell). At 8 C, however, the Li_xSi -cell was less able to withstand the high current and only reached a Q_{CC}/Q_{CCCV} -ratio of 40.5%, while the Si-cell was able to still maintain to charge 46.7% of the remaining capacity during the CC-phase. This difference is quite astonishing, since the Si-cell already significantly aged, and therefore, experienced an even greater C-rate than 8 C. To understand the reason for this discrepancy in C-rate capability, it is important to investigate the voltage curve (Figure 7C,D) at different currents.

From 0.5 till 2 C, the dis-/charging patterns of both cells display similar patterns with the main difference being the reduced capacity for the Si-cell. However, when a current of 4 C is applied, the Li_xSi -cell experiences in the beginning a stronger increase in voltage compared to the Si-cell, revealing a difference in terms of overpotential between both cells. This effect is even enhanced when observing the voltage curve at 8 C, suggesting the presence of different limitations for both cells during the lithiation process.

One would assume that this scenario may only occur the other way around, since the preliminary integration of Li should result in an increased Li-ion conductivity inside the Li_xSi anode compared to the Si anode, allowing for an improved lithiation of the anode. While this can also be the case as shown by another cell measurement (Figure S9, Supporting Information), here, the circumstance of inhomogeneous prelithiation may have resulted in an increased amount of Li present at the separator|anode interface.

This high Li concentration can obstruct the homogenous lithiation of the anode, hence, increasing the overpotential during lithiation. Since the same applies to the discharge, an increased amount of Li in the Li_xSi anode exists most likely deep inside the core of the particle, making its removal especially at high C-rates unlikely. Therefore, it functions as a barrier, reducing the de-/lithiation rate of the Li_xSi anode.

Upon finishing the C-rate capability testing, both cells show nearly identical response in comparison to the start when cycled once more at 0.5 C. This suggests that the cells experienced minimal damage during the testing. However, to check the overall health of both cells after cycling and C-rate capability testing, the cells were slowly (0.2 C) dis-/charged in cycle 137 (7th energy test). The resulting change in Q_{DCh} -retention shows that the Li_xSi -cell (98.4%) only aged slightly, during both periods. The Si-cell, however, strongly aged during cycling but remained stable during C-rate capability testing (85.8%). For additional information about the ageing process, EIS (Figure 8) at 4.20 V (Si-cell) and 4.25 V (Li_xSi -cell) were recorded in cycle 137 and compared to

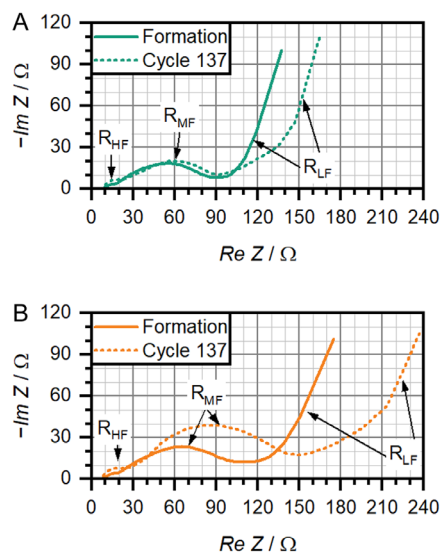


Figure 8. Recorded EIS data of the A) Si- and B) Li_xSi -cell during formation (line) and cycle 137 (dashed line) at 4.20 V (Si-cell) and 4.25 V (Li_xSi -cell). All cells were tested at 50 °C.

the EIS data during formation. For the analysis, the EIS data was segmented into high frequency (HF), medium frequency (MF), and low frequency region. In the HF region, both cells show a noticeable increase in impedance. Since this region mainly describes the charge transfer between the solid electrolyte particles, the quite slight change in both cases can be associated to the restructuring of the anode. During restructuring, the anode can selectively lose contact to the separator, which inevitably leads to an increase in impedance. In the MF region, no meaningful change can be noticed for the Si-cell. When observing the MF region of the Li_xSi -cell, however, a strong increase in the charge-transfer signals can be observed. This change is quite surprising, considering that the cell only aged slightly in terms of Q_{DCh} -retention during cycling and C-rate capability testing. However, its existence adds additional explanation to the observed lack in performance during 8 C testing. Since the deviation only occurs in the Li_xSi anode, the reason for the increased impedance has to be connected to the interphase between the separator and Li_xSi anode, indicating the formation of a barrier, which is capable to limit the Li-ion flow in this area.

Starting the rapid ageing at 4 C, both cells reach a Q_{CC}/Q_{CCCV} -ratio of $\approx 70\%$, which is slightly below the measured ones in the C-rate capability test.

However, during continuous testing in the harsh conditions, the Si-cell continues the previous ageing pattern, and additionally, is being affected by an increase in overpotential, reducing the ability to maintain 70% in Q_{CC}/Q_{CCCV} -ratio. Already during the 8th energy test (cycle 238), the cell is only able to reach a Q_{DCh} -retention of 77.94%, marking its end-of-life (EOL), when compared to commercial standards (limit: 80%). However, when examining the impact of the harsh conditions on the Li_xSi -cell, the effect is far more severe. Accompanied by a strong decrease of the Q_{CC}/Q_{CCCV} -ratio, the Li_xSi -cell faced accelerated ageing compared to previous cycling. Thus, leading to a decrease in Q_{DCh} -retention to 81.65%, barely exceeding the EOL limit, after the

9th energy test (cycle 339). Additionally, at this point the Q_{CC}/Q_{CCCV} -ratio already dropped to 36.73%, hinting at a kinetic limitation occurring in the cell. In direct comparison to the Si-cell, the rate of degradation is substantially increased, eventually resulting in the converging of both curves. After the 10th energy test (cycle 440), the Q_{DCH} -retention for the Si- and Li_xSi -cell remains at 70.13% and 76.40% with a Q_{CC}/Q_{CCCV} -ratio of 50.08% and 19.74%, respectively. In conclusion, although the Li_xSi -cell was initially stable, the change of current to 4 C resulted in an accelerated ageing of the cell, which was not observed for the Si-cell. Therefore, this effect is linked to the Li_xSi anode and reveals a fundamental challenge to overcome when integrating Li_xSi as anode active material.

3. Conclusion

In summary, this work displays an approach for sustainable chemical prelithiation of Si powder using a carrier-type reaction. Via the combination of various method (IR, Raman, SXES, ICP-OES), successful but inhomogeneous prelithiation, which was most likely caused by missing thermodynamical limits, was proven. Additionally, the recovery of unchanged TMBP after the prelithiation process confirmed the carrier role of the arene and demonstrate the sustainable character of the approach. However, due to the vigorous reactivity of the Li_xSi material with H_2O (see Figure S2, Supporting Information), scalability of this procedure needs to be carefully reviewed. For instance, a study conducted by Kuo et al., already tested a potential scale-up in a similar process but rely on SiO_2 containing material and surface passivation agent to increase stability against H_2O .^[24]

Nevertheless, due to a fully inert processing, unchanged Li_xSi containing electrodes were able to be manufactured. This allowed not only to observe an improved compressibility of the Li_xSi particles but also to investigate the electrochemical properties of the Li_xSi as an anode in an ASSB cell. The direct comparison to a pristine Si anode showed that the performance of Li_xSi -cells matches those of Si-cells but excels in cycle stability during 2 C cycling. However, at higher C-rates Li_xSi -cells experience a kinetic limitation, which when ongoing results in a rapid ageing of the cells. Since Si-cells did not show such limitation, this attribute can be linked to the Li_xSi material and may be affected by the predominant DOL.

In general, prelithiation is a powerful tool to enhance the electrochemical properties of Si. The approach presented here offers initial insights into a particle-based solution for incorporating this concept into ASSB. Despite revealing several challenges, the concept has proven beneficial for the cycle stability of ASSB with integrated electrolyte-free anodes, laying a solid foundation for future progress in this field.

4. Experimental Section

Prelithiation of the Silicon Powder

To produce the LAC reagent, 674 mg (3.20 mmol) of 3,3',4,4'-tetramethylbiphenyl (TMBP, 98%, crystalline powder, ThermoFisher

Scientific) was dissolved in 40 mL THF (99.85%, extra dry, stabilized, Thermo Scientific) and stirred for 5 min under Ar atmosphere. Adding 1.11 (160 mmol) g of Li metal grains (99%, granular, Sigma Aldrich) to the colorless solution resulted in teal blue coloring. After continuous stirring for 5 min, 9.00 g (320 mmol) of Si (microcrystalline, >99%, PCC Thorion GmbH) powder was added while stirring. The reaction solution was stirred over three consecutive days at room temperature until all Li was consumed. The progress of the reaction was monitored by observing the remaining floating Li grains. Upon completion, the solvent was removed i. vac. and a black powder was obtained. Residual TMBP was removed i. vac. at 150 °C and collected for further investigation. Products were stored in sealed glass containers under Ar atmosphere.

Electrode Fabrication and Cell Assembly

All manufacturing of electrodes and separators as well as cell assembly were performed inside an argon filled glovebox (E-Line, GS Glovebox System) at $O_2 < 1$ ppm and $H_2O < 1$ ppm.

To prepare electrolyte-free anode electrodes, a stock binder solution (10 wt%) of HNBR (TherbanLT1707, Acrylonitrile: 17 wt%, Arlanxco, dried at: <50 mbar, min. 12 h, 50 °C) in o-xylene (99%, extra dry, ThermoFisher Scientific) was prepared. By adding Si (microcrystalline, >99%, PCC Thorion GmbH) or Li_xSi powder to the stock binder and additional o-xylene (to adjust the viscosity) slurry (0.67 and 0.39 g ml^{-1} , respectively) was formulated at 15 Hz (Si) or 25 Hz (Li_xSi) for 1 or 0.5 h inside a mixer mill 500 nano (Retsch). Electrode slurry casting was performed using a doctor blade (wet coating thickness: 45 μm for Si and 80 μm for Li_xSi) and a film applicator on a copper foil (9 μm , MSE Supplies) to achieve an areal capacity of 2 mAh cm^{-2} assuming a specific capacity of 1910 and 1700 mAh g^{-1} for Si and Li_xSi (DOL = 0.5), respectively, ensuring an effective transport of two electrons per Si. After casting, the electrodes were dried at room temperature inside the glovebox for one hour and subsequently for at least 30 min in vacuum. Dried anodes were cut to a 5.8×4.5 cm^2 format to determine the areal density of 1.0 mg cm^{-2} (Si anode) and 1.2 mg cm^{-2} (Li_xSi anode). It should be noted that the copper foil possesses a declared areal density of 8.5–9.0 mg cm^{-2} (margin of error: ± 0.27 mg cm^{-2}), which significantly impacts the actual mass loading of the Si or Li_xSi electrode. Slurry formulation for cathodes consisting of 79.2 wt% single crystal $Ni_{0.6}Mn_{0.2}Co_{0.2}O_2$ (NMC622, D50: 3–6 μm , MSE Supplies, dried at: <50 mbar, min. 12 h, 150 °C), 19.8 wt% Li_6PS_5Cl , and 1 wt% HNBR was performed via wet-milling similar the one used for the Si electrode slurries. To achieve an areal capacity of ≈ 2 mAh cm^{-2} (assuming a specific discharge capacity of 160 mAh g_{NMC622}^{-1}), cathode slurries were casted onto an aluminum foil (12 μm , MSE Supplies) using the doctor blade method (wet coating thickness: 240 μm). Dried cathodes were cut to a 5.8×4.5 cm^2 format to determine the average areal mass loading of 14.68 mg cm^{-2} . It should be noted that due to small-scale processing individual sheets or spots inside one sheet may differ. Therefore, cathodes were selected to fit within a 10% range of the average mass loading.

The thin separator layer (≈ 30 μm) was prepared by infiltration of a PET nonwoven (Freudenberg Technology) from both sides via doctor blade casting with a dispersion consisting of 98 wt% Li_6PS_5Cl and 2 wt% HNBR (taken from stock solution) dispersed in o-xylene (≈ 0.95 g $_{LPSCl}$ ml^{-1}).

Cells were assembled in an ASC–A(+) cell casing (Sphere Energy) with either a polyetherimide (PEI) or a polyether ether ketone (PEEK) cell body and insulation sleeve (Sphere Energy). Electrode coins were punched to a diameter of 8 mm (anode and separator) or 7 mm (cathode) and centered stacked in the insulation sleeve (stacking order: stainless steel plate ($d = 8$ mm, $th = 0.5$ mm), anode, separator, cathode), followed by pressing the stack with a force of 5 kN. Then, a PTFE O-ring ($th = 100$ μm , $d_o = 8$ mm, $d_i = 7.2$ mm) was placed around the cathode, a second metal plate was placed

on top, and the stack was pressed with a force of 20 kN. Afterwards, three coins made of aluminum foil ($d = 8$ mm, $th = 12\text{--}15$ μm) were placed between the cathode and the upper metal plate for improved contacting and a homogeneous pressure distribution on the cell. Figure S8, Supporting Information, shows a schematic overview of the assembled battery cell. The sleeve was then assembled into the cell casing and closed by tightening six screws (Quality: 12.9) slightly. After heating the cell to 50 °C for at least one hour, the upper screws were tightened using a torque of 5.8 Nm to ensure a tight fit. For each material two cells were assembled and characterized. In case of differences between the individual cells, the best matching (based on individual NMC622 mass) was chosen for the overall comparison. All cells are shown in Figure S9,S10 (Supporting Information).

Electrochemical Characterization

Electrochemical measurements were performed on a Neware BTS4000 series battery tester at 50 °C in a potential window of 2.5–4.2 V (Si-cell) or 4.25 V (Li_xSi -cell). Formation of the cells was performed by constant current constant voltage (CCCV) dis-/charging at a current of 38.6 mA g_{NMC622}^{-1} and a cut-off at 19.3 mA g_{NMC622}^{-1} . The resulting discharge capacity (Q_{DCh}) was determined and used for defining the C-rate ($1\text{ C} = Q_{\text{DCh}}\text{ h}^{-1}$). Following the initial charging, the cells were rested for at least 5 h. Afterwards, recharged and hold at the respective upper cut-off voltage until a cut-off of 20 μA was reached, ensuring a pseudo thermodynamic equilibrium of the cells. At a bias of 4.2 or 4.25 V, EIS was performed in the range of 12 MHz–10 mHz (20 steps/dec (10 times/step) above 66 Hz, 2 steps/dec (2 times/step) below 66 Hz) using a Zahner Zennium X. Obtained data were refined to 6 MHz–10 mHz using the software Zahner Analysis 3.2.1. After the EIS measurement, the cells were discharged at the C-rates given above.

Cycling of the cells was performed in five intervals of 20 cycles each, with a CCCV charge and discharge at 2 C (cut-off: 0.2 C). Before and after these intervals, an energy test was conducted with a CCCV charge at 2 C (cut-off: 0.2 C) and a CCCV discharge at 0.2 C (cut-off: 0.1 C). Following the five interval cycles a C-rate capability test was conducted with CCCV charge and discharge for five cycles each at 0.5, 1, 2, 4, 8, and 0.5 C (cut-off: 0.2 C) and finished by a charging at 0.2 C (cut-off: 0.1 C), including EIS measurement at 4.2 or 4.25 V (parameters were set identical to the measurement in the formation cycle). Selected cells were then discharged at 0.2 C (cut-off: 0.1 C) followed by a rapid ageing test with a CCCV dis-/charge at 4 C (cut-off: 0.2 C). After every 100 cycles, an energy test was performed with a CCCV charge at 4 C (cut-off: 0.2 C) and a CCCV discharge at 0.2 C (cut-off: 0.1 C). The discharge capacities of the energy test were considered for the determination of the capacity retention of the cells.

Physicochemical Characterization Methods

Cross-sections of the cell stacks were prepared by precutting an ASSB cell (ready for formation) with a scalpel under Ar atmosphere. Afterwards, the pre-cut cell stack was placed into a special sample holder and adjusted to remove 100 μm of the freshly cut cross-section. To prepare polished cross-sections of the cell stacks, all samples were transferred via an inert shuttle into a cryo-cross section polisher (CCP, JEOL IB-19 520) and milled at -110 °C, using an Ar ion beam with an accelerating voltage of 4 kV for 4.5 h (gas flow 2.4–2.8).

SEM images were recorded using a JEOL JSM-IT800 Schottky field emission scanning electron microscope with a back-scattered electron detector at a working distance of 10 mm and an acceleration voltage of 15 kV. Air sensitive samples were transferred via an inert shuttle into the SEM.

EDX-mapping was performed with an Oxford Ultim Max 100 EDX (SDD size: 100 mm^2) detector using an acceleration voltage of 15 kV and a fixed working distance at 10 mm.

For SXES measurements, the working distance of the SEM was fixed at 10 mm. An accelerating voltage of 5 kV was applied. The beam current and the acquisition time were set to 50 nA and 300 s, respectively.

A HORIBA XploRa Plus Raman spectrophotometer with a confocal microscope was used to analyze the electrolyte-free anode with a 532 nm laser. The power was set to 1% mW and spectra from 50–1500 cm^{-1} with an 1800 gr mm^{-1} grating were recorded with a measurement time of 60 s.

ATR-IR spectroscopy was performed using a Bruker Alpha II Fourier-transform infrared spectrometer with a spectral resolution of 4 cm^{-1} and 32 repetitive scans per background and sample measurement from 400 to 4000 cm^{-1} . Average values of triplicate measurements were used for the analysis. The acquired spectra for the air-treated Li_xSi were modified using a polynomial baseline correction in OPUS software (Bruker).

For ICP-OES measurements, part of the Li_xSi was quenched in 5 mL of deionized water. Afterwards, residual particles were removed using a syringe filter (pore size = 0.45 μm) and 0.15 mL of the solution was diluted to 50 mL using a 3 mol% HNO_3 standard solution. Afterwards, the sample was measured three times with an Analytik jena PlasmaQuant 9100 ICP-OES and an average concentration was calculated.

Acknowledgements

T.N. and A.T.C. contributed equally to this work. Parts of this work were financially supported by Vector Stiftung within the framework of Projekt NESSL. Additionally, the authors also thank PCC Thorion GmbH for supporting this work by providing the used silicon powder.

Open Access funding enabled and organized by Projekt DEAL.

Conflict of Interest

The authors declare no conflict of interest.

Data Availability Statement

The data that support the findings of this study are available from the corresponding author upon reasonable request.

Keywords: all-solid-state batteries · chemical prelithiation · silicon · soft X-ray emission spectroscopy

- [1] D. Lee, H. Lee, T. Song, U. Paik, *Adv. Energy Mater.* **2022**, *12*, 2200948.
- [2] J.-M. Doux, Y. Yang, D. H. S. Tan, H. Nguyen, E. A. Wu, X. Wang, A. Banerjee, Y. S. Meng, *J. Mater. Chem. A* **2020**, *8*, 5049.
- [3] A. Banerjee, X. Wang, C. Fang, E. A. Wu, Y. S. Meng, *Chem. Rev.* **2020**, *120*, 6878.
- [4] X. Bai, Y. Duan, W. Zhuang, R. Yang, J. Wang, *J. Mater. Chem. A* **2020**, *8*, 25663.
- [5] J. Yi, S. Shi, Q. Liu, T. Yang, *J. Power Sources* **2024**, *602*, 234370.
- [6] W. Zhao, J. Yi, P. He, H. Zhou, *Electrochem. Energ. Rev.* **2019**, *2*, 574.
- [7] T. Neumann, L. Alexander Dold, A. Thomas Cerny, E. Tröster, M. Günthel, A. Fischer, K. Peter Birke, I. Krossing, D. Biro, *Batteries Supercaps* **2025**, *8*, e202400412.
- [8] X. Zhang, Y. Yang, Z. Zhou, *Chem. Soc. Rev.* **2020**, *49*, 3040.
- [9] D. H. S. Tan, Y.-T. Chen, H. Yang, W. Bao, B. Sreenarayanan, J.-M. Doux, W. Li, B. Lu, S.-Y. Ham, B. Sayahpour, J. Scharf, E. A. Wu, G. Deysher, H. E. Han, H. J. Hah, H. Jeong, J. B. Lee, Z. Chen, Y. S. Meng, *Science* **2021**, *373*, 1494.

- [10] S. Chae, S.-H. Choi, N. Kim, J. Sung, J. Cho, *Angew. Chem. Int. Ed. Engl.* **2020**, *59*, 110.
- [11] G. Zhu, D. Chao, W. Xu, M. Wu, H. Zhang, *ACS nano* **2021**, *15*, 15567.
- [12] H. Wu, G. Chan, J. W. Choi, I. Ryu, Y. Yao, M. T. McDowell, S. W. Lee, A. Jackson, Y. Yang, L. Hu, Y. Cui, *Nat. Nanotechnol.* **2012**, *7*, 310.
- [13] S. Poetke, F. Hippauf, A. Baasner, S. Dörfler, H. Althues, S. Kaskel, *Batteries Supercaps* **2021**, *4*, 1323.
- [14] J. Jang, I. Kang, J. Choi, H. Jeong, K.-W. Yi, J. Hong, M. Lee, *Angew. Chem. Int. Ed. Engl.* **2020**, *59*, 14473.
- [15] J. Choi, H. Jeong, J. Jang, A.-R. Jeon, I. Kang, M. Kwon, J. Hong, M. Lee, *J. Am. Chem. Soc.* **2021**, *143*, 9169.
- [16] G. Wang, F. Li, D. Liu, D. Zheng, Y. Luo, D. Qu, T. Ding, D. Qu, *ACS Appl. Mater. Interfaces* **2019**, *11*, 8699.
- [17] Y. Li, L. Lv, R. Liang, L. Wang, Y. Wang, Q. Qu, M. Shen, H. Zheng, *J. Mater. Chem. A* **2024**, *12*, 20045.
- [18] E. Adhitama, F. Dias Brandao, I. Dienwiebel, M. M. Bela, A. Javed, L. Haneke, M. C. Stan, M. Winter, A. Gomez-Martin, T. Placke, *Adv. Funct. Mater.* **2022**, *32*, 2201455.
- [19] A. V. Bhujbal, K. L. Ng, S. Khazraei, J. Bekou, A. R. Riahi, *J. Electrochem. Soc.* **2023**, *170*, 80506.
- [20] Z. Fan, B. Ding, Z. Li, Z. Chang, B. Hu, C. Xu, X. Zhang, H. Dou, X. Zhang, *eTransportation* **2023**, *18*, 100277.
- [21] L. Jin, C. Shen, Q. Wu, A. Shellikeri, J. Zheng, C. Zhang, J. P. Zheng, *Adv. Sci.* **2021**, *8*, e2005031.
- [22] G. W. Canters, E. de Boer, *Mol. Phys.* **1973**, *26*, 1185.
- [23] Y. Shen, X. Shen, M. Yang, J. Qian, Y. Cao, H. Yang, Y. Luo, X. Ai, *Adv. Funct. Mater.* **2021**, *31*, 2101181.
- [24] C. Kuo, H. Hsu, C. Lan, *J. Power Sources* **2023**, *558*, 232599.
- [25] M. Graf, C. Berg, R. Bernhard, S. Haufe, J. Pfeiffer, H. A. Gasteiger, *J. Electrochem. Soc.* **2022**, *169*, 20536.
- [26] B. Vasconcelos, R. Serra, J. Oliveira, C. Fonseca, *Coatings* **2020**, *10*, 1237.
- [27] B. S. Parimalam, A. D. MacIntosh, R. Kadam, B. L. Lucht, *J. Phys. Chem. C* **2017**, *121*, 22733.
- [28] J. R. Ferraro, M. H. Manghnani, L. J. Basile, *J. Appl. Phys.* **1973**, *44*, 5391.
- [29] T. Fuss, A. Mogaš-Milanković, C. S. Ray, C. E. Leshner, R. Youngman, D. E. Day, *J. Non-Cryst. Solids* **2006**, *352*, 4101.
- [30] S. Shin, A. Agui, M. Watanabe, M. Fujisawa, Y. Tezuka, T. Ishii, *Phys. Rev. B Condens. Matter* **1996**, *53*, 15660.
- [31] H. Lin, K. Uosaki, H. Noguchi, *Appl. Surf. Sci.* **2021**, *569*, 151040.
- [32] L. A. Berla, S. W. Lee, Y. Cui, W. D. Nix, *J. Power Sources* **2015**, *273*, 41.
- [33] J. Song, M. Zhou, R. Yi, T. Xu, M. L. Gordin, D. Tang, Z. Yu, M. Regula, D. Wang, *Adv. Funct. Mater.* **2014**, *24*, 5904.

Manuscript received: April 30, 2025

Revised manuscript received: June 11, 2025

Version of record online: